J. Fluid Mech. (2019), *vol.* 873, *pp.* 1055–1071.
doi:10.1017/jfm.2019.446

Convective heat transfer along ratchet surfaces in vertical natural convection

Hechuan Jiang[1], Xiaojue Zhu[2], Varghese Mathai[3], Xianjun Yang[1], Roberto Verzicco[4,5], Detlef Lohse[5,6] and Chao Sun[1,5,†]

[1]Center for Combustion Energy, Key Laboratory for Thermal Science and Power Engineering of Ministry of Education, Department of Energy and Power Engineering, Tsinghua University, 100084 Beijing, China

[2]Center of Mathematical Sciences and Applications, and School of Engineering and Applied Sciences, Harvard University, Cambridge, MA 02138, USA

[3]School of Engineering, Brown University, Providence, RI 02912, USA

[4]Dipartimento di Ingegneria Industriale, University of Rome 'Tor Vergata', Via del Politecnico 1, 00133 Roma, Italy

[5]Physics of Fluids Group and Max Planck Center Twente, University of Twente, PO Box 217, 7500AE Enschede, The Netherlands

[6]Max Planck Institute for Dynamics and Self-Organization, 37077 Göttingen, Germany

(Received 29 January 2019; revised 28 May 2019; accepted 29 May 2019; first published online 28 June 2019)

We report on a combined experimental and numerical study of convective heat transfer along ratchet surfaces in vertical natural convection (VC). Due to the asymmetry of the convection system caused by the asymmetric ratchet-like wall roughness, two distinct states exist, with markedly different orientations of the large-scale circulation roll (LSCR) and different heat transport efficiencies. Statistical analysis shows that the heat transport efficiency depends on the strength of the LSCR. When a large-scale wind flows along the ratchets in the direction of their smaller slopes, the convection roll is stronger and the heat transport is larger than the case in which the large-scale wind is directed towards the steeper slope side of the ratchets. Further analysis of the time-averaged temperature profiles indicates that the stronger LSCR in the former case triggers the formation of a secondary vortex inside the roughness cavity, which promotes fluid mixing and results in a higher heat transport efficiency. Remarkably, this result differs from classical Rayleigh–Bénard convection (RBC) with asymmetric ratchets (Jiang *et al.*, *Phys. Rev. Lett.*, vol. 120, 2018, 044501), wherein the heat transfer is stronger when the large-scale wind faces the steeper side of the ratchets. We reveal that the reason for the reversed trend for VC as compared to RBC is that the flow is less turbulent in VC at the same *Ra*. Thus, in VC the heat transport is driven primarily by the coherent LSCR, while in RBC the ejected thermal plumes aided by gravity are the essential carrier of heat. The present work provides opportunities for control of heat transport in engineering and geophysical flows.

Key words: Bénard convection, turbulent convection

† Email address for correspondence: chaosun@tsinghua.edu.cn

1. Introduction

Thermally driven flows play an important role in nature and in many industrial applications; examples are convection in the oceans and atmosphere, in the ventilation of buildings and in the cooling of devices. In most of these cases, the conducting surfaces are generally not smooth. As a paradigm for the study of thermal turbulence, Rayleigh–Bénard convection (RBC) – a fluid layer heated from below and cooled from above – has been studied extensively in the past few decades (for reviews, see e.g. Ahlers, Grossmann & Lohse 2009; Lohse & Xia 2010; Chillà & Schumacher 2012). A related but distinctly different model problem can be considered when the cooling and heating are applied to the vertical side walls, rather than to top and bottom plates. This system was referred to as a 'differentially heated cavity' in Batchelor (1954), and there are a large number works on this topic (Patterson & Imberger 1980; Paolucci & Chenoweth 1989; Xin & Le Qur 1995; Dol & Hanjalic 2001; Xu, Patterson & Lei 2009; Yousaf & Usman 2015; Dou & Jiang 2016; Belleoud, Saury & Lemonnier 2018). However in the current paper, in order to emphasize the difference between this system and RBC, we prefer to refer to it as vertical natural convection (VC) as adopted in Ng *et al.* (2015, 2017, 2018) and Shishkina (2016). An important feature of VC as compared to RBC is that gravity acts orthogonal to the heat flux, which happens frequently in nature, in building ventilation, in power plants and in electronic chip systems. Hence, enhancing the heat transport in this particular configuration can have great relevance in many applications.

To enhance the heat transfer in thermal convection, numerous strategies have been proposed, such as introducing wall roughness, nanofluids (Tiwari & Das 2007; Corcione 2010) or bubbles (Narezo Guzman *et al.* 2016; Gvozdić *et al.* 2018, 2019). Among these approaches, the introduction of symmetric wall roughness has been shown to be an efficient way to enhance the transfer properties. Hence, numerous experimental (Shen, Tong & Xia 1996; Du & Tong 1998, 2000; Roche *et al.* 2001; Qiu, Xia & Tong 2005; Tisserand *et al.* 2011; Salort *et al.* 2014; Xie & Xia 2017; Jiang *et al.* 2018), numerical (Stringano, Pascazio & Verzicco 2006; Yousaf & Usman 2015; Wagner & Shishkina 2015; Toppaladoddi, Succi & Wettlaufer 2017; Zhu *et al.* 2017; Jiang *et al.* 2018; Zhang *et al.* 2018) and theoretical (Villermaux 1998; Shishkina & Wagner 2011; Goluskin & Doering 2016) efforts have been made to explain and control the heat transfer in thermal convection with symmetrically rough walls, mainly in the context of RBC.

In addition to the widely explored case of symmetric roughness, a more general possibility is to use asymmetrically rough surfaces that resemble the classical Feynman–Smoluchoski ratchet (Smoluchowski 1912; Feynman, Leighton & Sands 1963). Several experimental and numerical investigations have employed the Feynman–Smoluchoski ratchet-like roughness in various problems, all leading to a breaking of the symmetry of the system. These include self-propelled Leidenfrost droplets and solids on ratchet surfaces (Linke *et al.* 2006; Lagubeau *et al.* 2011), 'capillary ratchets' in feeding by birds (Prakash, Quéré & Bush 2008) and even 'Brownian ratchets' of molecular motors (Van Oudenaarden & Boxer 1999; Hänggi & Marchesoni 2009). In the context of RBC, Jiang *et al.* (2018) recently found that ratchet-like roughness induces symmetry breaking and thereby a preferred orientation of the large-scale circulation and pronounced difference in heat transfer, depending on whether the large-scale roll sweeps along or against the ratchet direction.

In the present work, we conduct a combined experimental and numerical study of the influence of ratchet-like (asymmetric) wall roughness on heat transfer and flow dynamics in VC, in particular on the large-scale circulation roll (LSCR). Similar to

the definitions in RBC, the relevant parameters in VC are: the Rayleigh number Ra – the dimensionless temperature difference between hot and cold vertical walls; the Prandtl number Pr – the ratio of momentum diffusivity to thermal diffusivity; and as a response of the system the Nusselt number Nu – the dimensionless specific heat flux. These are defined as

$$Ra = \frac{\alpha g H^3 \Delta}{\nu \kappa}, \quad Pr = \frac{\nu}{\kappa} \quad \text{and} \quad Nu = \frac{J}{(\chi \Delta / H)}, \tag{1.1a–c}$$

where α, g, H, Δ, ν, κ, χ and J are the thermal expansion coefficient, gravitational acceleration, thickness of the fluid layer between the conducting plates, temperature difference between hot (T_h) and cold (T_c) plates, kinematic viscosity, thermal diffusivity, thermal conductivity of the convecting fluid and heat flux per unit area, respectively.

In Jiang *et al.* (2018), it was shown that in RBC the two different orientations of the LSCR over the asymmetric roughness structures gave different heat transport properties. This could be connected to the dynamics of plume emissions. The case in which the flow near the top and bottom plates moves along the smaller slope side of the ratchets (case A) gives a smaller Nu enhancement compared to the case in which the flow near the top and bottom plates travels against the steeper slope side of the ratchets (case B), as in the latter case, additional plume emission is triggered.

How do these two cases compare in VC? Recent work (Ng *et al.* 2015, 2018) suggests that many of the flow features in VC are similar to those of RBC, such as the laminar-like scaling for the boundary layer thickness of velocity and temperature, the kinetic and thermal dissipations in the boundary layers and so on. Besides, the studies of VC with symmetric surface structures such as fins (Xu *et al.* 2009), squares (Shakerin, Bohn & Loehrke 1988) and sinusoidal roughness (Yousaf & Usman 2015) also show similar phenomena and properties to RBC with symmetric rough conducting plates. Does this also mean that the effects of asymmetric ratchet structures on the heat transport and flow dynamics are also similar for VC and RBC? Answering these questions will be the objective of the present study.

The paper is organized as follows. We first describe the experimental set-up and numerical methods in § 2, which is divided into three subsections. Geometrical aspects of the convection cell, temperature monitoring techniques and shadowgraph visualization techniques are described in §§ 2.1–2.2. Section 2.3 introduces the numerical methods. Section 3 presents the results and analyses performed, with regard to the effects of ratchet structures on the heat transport efficiencies (§ 3.1), the dynamics of LSCR (§ 3.2) and the properties of temperature profiles (§ 3.3). In § 3.4 we highlight the differences in the heat transport in VC and RBC systems with ratchet structures. Final remarks and conclusions are given in § 4.

2. Experimental set-up and direct numerical simulations

2.1. *Convection cell*

Experiments are performed in a rectangular cell (see figure 1*a*), with ratchet structures on the hot and cold vertical conducting plates.

The conducting plates are made of copper, and their surfaces are electroplated with a thin layer of nickel to prevent oxidation. The sidewall of the cell is made of transparent Plexiglas for flow visualization. The length (L), width (W) and height (H) of the cell are 240, 60 and 240 mm, respectively, resulting in a unit aspect ratio

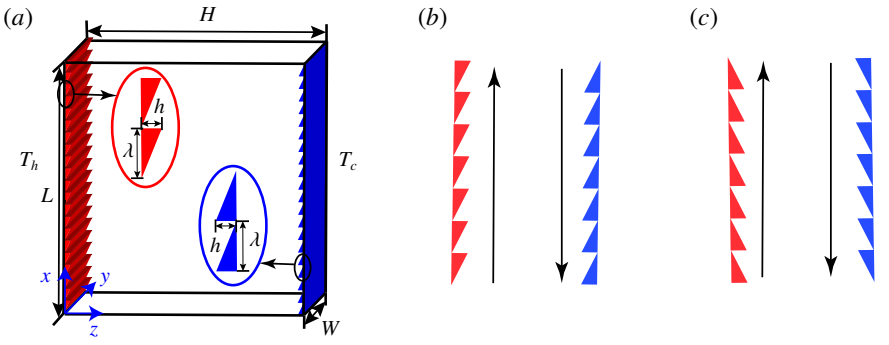

FIGURE 1. (Colour online) (*a*) A sketch of a convection cell with asymmetric ratchets on vertical side plates. (*b*) Schematic showing the flow configuration where the LSCR moves along the smaller slope side of the ratchets, referred to subsequently as VC-case-A. (*c*) Schematic of the flow configuration where the LSCR travels towards the steeper slope of the ratchets, subsequently referred to as VC-case-B.

in the large-scale circulation plane ($\Gamma \equiv L/H = 1$). Two silicone rubber film heaters, which are supplied by DC power with a 0.05 % long-term stability, are sandwiched in the hot plate to provide constant heat flux. The cold vertical plate is connected to a cooling chamber, which is regulated at constant temperature by circulating cold water from a temperature-controlled circulating bath (Polyscience, PP15R-40-A12Y). The temperature stability of the circulating bath is 0.005 K within the experimental temperature range, and the maximum cooling power is 1 kW. In our experiments, there are two opposing inlets and two opposing outlets at the side of the chamber to keep the temperature of the cold plate as uniform as possible. It should be pointed out that the temperature boundary condition is constant temperature for cold plate and constant heat flux for hot plate in our experiments. In the RBC system, at high *Ra*, the difference of global heat transport between constant-temperature and constant-heat-flux boundary conditions is almost negligible (Johnston & Doering 2009; Huang *et al.* 2015). However in the VC system, there is a small difference in global heat transfer between the two temperature boundary conditions, which will be discussed in § 3.1.

The ratchet-like structures on the hot and cold vertical plates each have a height $h = 6$ mm and the wavelength $\lambda = 12$ mm. In our experiments, the situation in which the flow near the hot and cold plates moves along the smaller slope side of the ratchets is subsequently referred to as VC-case-A (see figure 1*b*). When the relative flow direction is reversed, i.e. when the flow near the hot and cold plates travels towards the steeper slope of the ratchets, we refer to this flow configuration as VC-case-B (see figure 1*c*). For comparison, we have also studied a cell with smooth hot and cold plates, which is subsequently referred to as VC-smooth.

To study the heat transport over a wide *Ra* range, we use two working fluids: (i) distilled water and (ii) Novec 7200 (Novec 7200 Engineered Fluid, 3M Inc.). The detailed properties for the two fluids are listed in table 1. In our experiments, for distilled water the temperature of the bulk fluid is maintained at $40 \pm 0.05\,^{\circ}\mathrm{C}$, resulting in a corresponding Prandtl number $Pr = 4.3$. In comparison, Novec 7200 is maintained at a temperature of 25 °C, for which $Pr = 10.7$.

The convection cell is wrapped up with a 5 cm thickness of Styrofoam to minimize heat leakage to the surroundings. To further prevent heat leakage, a PID-controlled

	T (°C)	χ (W m^{-1} K^{-1})	α ($\times 10^{-4}$ K^{-1})	ν ($\times 10^{-7}$ m^2 s^{-1})	c_p (J kg^{-1} K^{-1})	ρ (kg m^{-3})
Water	40	0.63	3.85	6.58	4178	992
Novec 7200	25	0.069	1.58	4.27	1214	1430

TABLE 1. Properties of working fluid for water at 40 °C and Novec 7200 at 25 °C.

temperature-regulated aluminium basin is placed on the left of the heating plate so that the temperature difference between the heating plate and environment is minimized. Furthermore, we use a constant-temperature bath controlled by PID to keep the temperature of the outside environment the same as the bulk temperature. In this way, almost all the heat produced by the heaters is transported through fluid to the cooling plate. Consequently, the net heat flux could be calculated as the electric power consumed, which is determined from the applied voltage and current to the heating films.

2.2. *Measurement techniques*

The temperature of the heating plate is measured using six thermistors (Omega, 44131), which are embedded in the heating plate. The locations of the thermistors are 20, 60, 100, 140, 180 and 200 mm away from the bottom edge of the cell. Another six thermistors are used to measure the temperature of the cooling plate at mirrored locations of the cooling plate. The thermistor has a room temperature resistance of 10 kΩ and is calibrated individually with an accuracy of 0.005 K using a circulating bath. We use the Steinhart–Hart equation (Lavenuta 1997) to convert the resistance of thermistors measured by a $6\frac{1}{2}$-digit multimeter (Keithley, 2701) to temperature.

As described in Jiang *et al.* (2018), shadowgraphy is used to visualize the flow structures. A white light-emitting diode light is passed through a Fresnel lens to form a uniform and parallel light source. The parallel light passing through the cell will converge or diverge according to the varying degree of refraction inside the fluid, which is a function of fluid temperature. A sheet of wax-paper is used as a projection screen for the shadowgraph, which is recorded using a Nikon camera. In order to minimize effects due to optical imperfections, the shadowgraph image is subtracted by an averaged background image pixel by pixel.

2.3. *Numerical methods*

We carry out three-dimensional direct numerical simulations in a rectangular cell using the second-order finite difference code AFiD (Verzicco & Orlandi 1996; van der Poel *et al.* 2015; Zhu *et al.* 2018), in combination with an immersed-boundary method (Fadlun *et al.* 2000) to track the ratchet structures. The code has been extensively validated in prior work (Zhu *et al.* 2017, 2018; Jiang *et al.* 2018). The governing Boussinesq equations in dimensionless forms read

$$\frac{\partial \boldsymbol{u}}{\partial t} + \boldsymbol{u}\cdot\boldsymbol{\nabla}\boldsymbol{u} = -\boldsymbol{\nabla} p + \sqrt{\frac{Pr}{Ra}}\nabla^2\boldsymbol{u} + \theta\hat{\boldsymbol{z}}, \tag{2.1}$$

$$\boldsymbol{\nabla}\cdot\boldsymbol{u} = 0, \tag{2.2}$$

$$\frac{\partial \theta}{\partial t} + \boldsymbol{u}\cdot\boldsymbol{\nabla}\theta = \frac{1}{\sqrt{RaPr}}\nabla^2\theta, \tag{2.3}$$

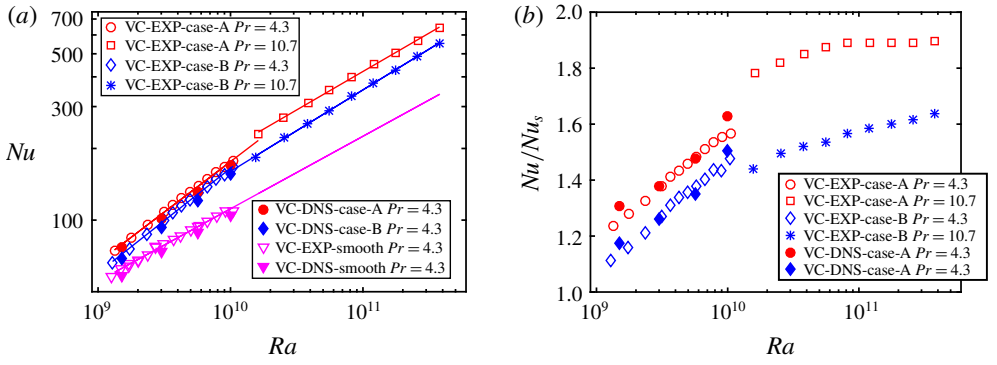

FIGURE 2. (Colour online) (*a*) Nusselt number Nu as a function of Rayleigh number Ra in the smooth and rough cells. (*b*) The Nu enhancement as a function of Ra for the two cases. The open symbols correspond to experimental data and the filled symbols correspond to numerical data.

Ra	Grid resolution ($N_x \times N_z \times N_y$)	Nu
	$640 \times 640 \times 128$	125.7
5.7×10^9	$1280 \times 1280 \times 256$	120.3
	$2560 \times 2560 \times 512$	120.1

TABLE 2. Grid convergence studies for VC-case-B at $Ra = 5.7 \times 10^9$.

where $\hat{z}$ is the unit vector pointing in the direction opposite to that of gravity, $\boldsymbol{u}$ the velocity vector normalized by the free-fall velocity $\sqrt{g\alpha\Delta H}$, t the dimensionless time normalized by $\sqrt{H/(g\alpha\Delta)}$, θ the temperature normalized by Δ and p the pressure normalized by $g\alpha\Delta/H$. As seen from the above equations, the control parameters for the system are the Rayleigh and Prandtl numbers. The material properties and the geometry of the cell were chosen to be the same as used in experiments. The no-slip boundary conditions were adopted for the velocity at all solid boundaries. At hot and cold plates constant temperatures were prescribed and at all other walls heat-insulating conditions were adopted. Adequate resolutions are ensured for all simulations so that the results are grid independent. For example, at $Ra = 5.7 \times 10^9$, $1280 \times 1280 \times 256$ grid points are used for the cases with ratchet. To verify the grid resolution, we have conducted a set of grid convergence studies for VC-case-B at $Ra = 5.7 \times 10^9$ as listed in table 2. Three grid resolutions have been tested, namely $640 \times 640 \times 128$, $1280 \times 1280 \times 256$ and $2560 \times 2560 \times 512$, and the resulting Nusselt numbers are 125.7, 120.3 and 120.1. Thus it is reasonable to choose the grid resolution $1280 \times 1280 \times 256$ for $Ra = 5.7 \times 10^9$.

3. Results and discussion

3.1. *Heat transport*

We first study the effects of ratchet structures on the convective heat transfer in VC. As mentioned in § 2.1, two kinds of working fluid are used for a wide Ra range. Figure 2(*a*) shows the measured Nu as a function of Ra for VC cases A, B and smooth. The experiments for rough cases covered a Ra range $[1.3 \times 10^9, 3.8 \times 10^{11}]$.

We expect that for the smooth case in such a Pr range [4.3, 10.7], the Nu dependence on Pr would be quite weak (Grossmann & Lohse 2001; Stevens, Lohse & Verzicco 2011) so that the results can be extrapolated to the whole Ra range and $Nu(Ra)$ can be described by a power law with an effective exponent of 0.30 ± 0.01. However, the Pr effect might manifest itself in the case of wall roughness. The reason is that if Pr is greater than one, with increasing Rayleigh number, the roughness element will first perturb the thermal boundary layer and then perturb the viscous boundary layer which might result in multiple regimes of Nusselt scalings. A detailed competition between roughness height and boundary layer thicknesses (thermal and viscous) will eventually determine the local scaling exponent at a specific Rayleigh number. This deserves systematic study in future to understand the particular Pr dependence in turbulent thermal convection with roughness.

Further, we find Nu for the rough wall cases is larger than that for the smooth wall case and two different scaling regimes exist as reported in Zhu *et al.* (2017). In regime I, corresponding to $Ra \in [1.3 \times 10^9, 1.0 \times 10^{10}]$, the roughness elements perturb the thermal boundary layers, resulting in dramatically enhanced heat transport. The local effective exponents are 0.42 ± 0.01 for VC-case-A and 0.44 ± 0.01 for VC-case-B. Upon further increasing Ra (up to 1.0×10^{10}), the scaling exponent saturates back to the effective value 0.32 ± 0.01 for VC-case-A and 0.34 ± 0.01 for VC-case-B, which we refer to as regime II. The numerical data are also plotted in figure 2(*a*). We find the experiments and simulations are in reasonable agreement, besides a marginal deviation in the absolute values. This small deviation can be attributed to the fact that in the numerical simulations, the temperature boundary conditions are constant temperature for both heating and cooling plates. However in our experiments, the temperature boundary conditions are mixed, with constant heat flux for the hot plate and constant temperature for the cold plate. For constant-heat-flux boundary condition, the thermal boundary layer develops along the heating surface, so there exists a temperature gradient along the heating plate. Indeed, at $Ra = 1.05 \times 10^{10}$, in the VC experiments we find a maximum temperature difference $\delta T/\Delta = 0.17$ on the hot plate. The different boundary conditions presumably cause the difference in Nu between experiments and numerical simulations.

To further demonstrate the Nu enhancement, we normalize the data in the ratchet-structure cell by Nu for the smooth case as shown in figure 2(*b*). Obviously, Nu is enhanced in both rough cases. The Nu enhancements for both cases have a similar trend: they are relatively small at the smallest $Ra \approx 10^9$, and increase with Ra monotonically. This occurs because with increasing Ra the thermal boundary layer thickness δ_T decreases, resulting in an increase in the effective roughness height h/δ_T (Zhu *et al.* 2017). Therefore, the roughness elements perturb the flow more strongly, which explains the increasing trend of the Nu enhancement with increasing Ra.

Next we focus on the difference in the Nu enhancements between the two rough cases. At the smallest $Ra = 1.3 \times 10^9$, Nu enhancement $Nu_{en} = 23.5\,\%$ for VC-case-A and $Nu_{en} = 11.2\,\%$ for VC-case-B. However, the Nu enhancements increase differently with increasing Ra for the two cases. At the highest $Ra = 3.8 \times 10^{11}$, Nu_{en} are $89.8\,\%$ and $63.6\,\%$ for VC-case-A and VC-case-B, respectively. What could be the physical mechanisms governing this huge difference in the Nu enhancement between the two cases? We will address this in the following section.

3.2. *Dynamics of large-scale circulation*

To study the mechanisms of distinct Nu enhancements for the two cases, we measure the wind Reynolds number Re as a function of Ra, where $Re = V_{LSC}H/\nu$, with

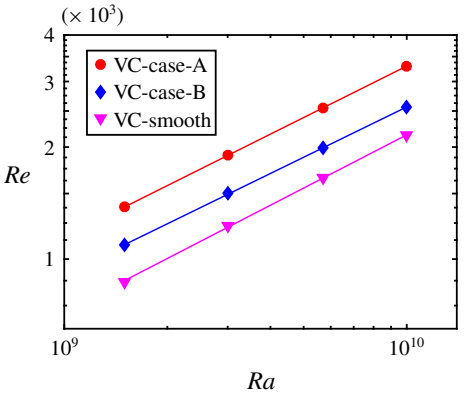

FIGURE 3. (Colour online) Reynolds number Re as a function of the Rayleigh number Ra. The Re is defined as $Re = V_{LSC}H/\nu$, where $V_{LSC} = (\langle u_x \rangle_S)_{max}$ is the maximum mean vertical velocity of LSCR.

$V_{LSC} = (\langle u_x \rangle_S)_{max}$ the maximum vertical mean velocity of LSCR. Here the notation $\langle \cdot \rangle_S$ denotes the average over time and over (any) vertical plane. As evident from figure 3, VC-case-A has the highest Re, followed by VC-case-B, and then the smooth case. The higher Re in VC-case-A should be responsible for the higher heat transport efficiency than VC-case-B. However, what causes the difference in flow intensity for the two rough cases?

To further elucidate the influence of the ratchet structures on the flow dynamics, we perform shadowgraph visualization at $Ra = 5.7 \times 10^9$ and $Pr = 4.3$. Figure 4(*a*,*d*) shows shadowgraph images for the two cases. For VC-case-A, the flow near the wall moves along the smaller slope side of the ratchets. In contrast, for VC-case-B (see figure 4*d*), the sharp corners of the ratchets slow down the LSCR, resulting in weaker convection. Figures 4(*b*) and 4(*e*) show instantaneous dimensionless temperature fields at $Ra = 5.7 \times 10^9$ and $Pr = 4.3$ for VC-case-A and VC-case-B, respectively. Consistent with the shadowgraph images, in VC-case-A the thermal plumes sweeping over the smaller slope of the ratchet elements are organized together to form a strong LSCR. In contrast, in VC-case-B the thermal plumes dissipate quickly due to the slowing down by the steeper slope of the ratchets, leading to a weaker LSCR. To further demonstrate the flow dynamics, we report the instantaneous dimensionless vertical velocity fields, shown in figure 4(*c*,*f*). For VC-case-A, the flow develops along the smaller slopes of the ratchets and is detached at the end of the wall to form a strong LSCR. However, the flow in VC-case-B is hindered by the sharp corners of the ratchets, and consequently results in lower LSCR velocities. This difference in the strength of the LSCR can be linked to the observed high heat transport efficiency of VC-case-A over VC-case-B.

Next, we quantify the strength of the LSCR for the two cases. Figure 5(*a*) shows the mean dimensionless vertical velocity as a function of position z/H. The mean vertical velocity profiles for both cases have a similar trend, with maximum values just beyond the ratchet tips. As is clear from the inset, VC-case-A has a higher maximum dimensionless mean vertical velocity $(\langle u_x \rangle_S)_{max}(A) = 0.072$ than VC-case-B, for which $(\langle u_x \rangle_S)_{max}(B) = 0.058$. Consistent with the instantaneous vertical velocity fields, the time-averaged vertical velocity fields reveal that for VC-case-A (figure 5*b*), the LSCR is stronger as compared to that for VC-case-B (figure 5*c*). Furthermore, a secondary

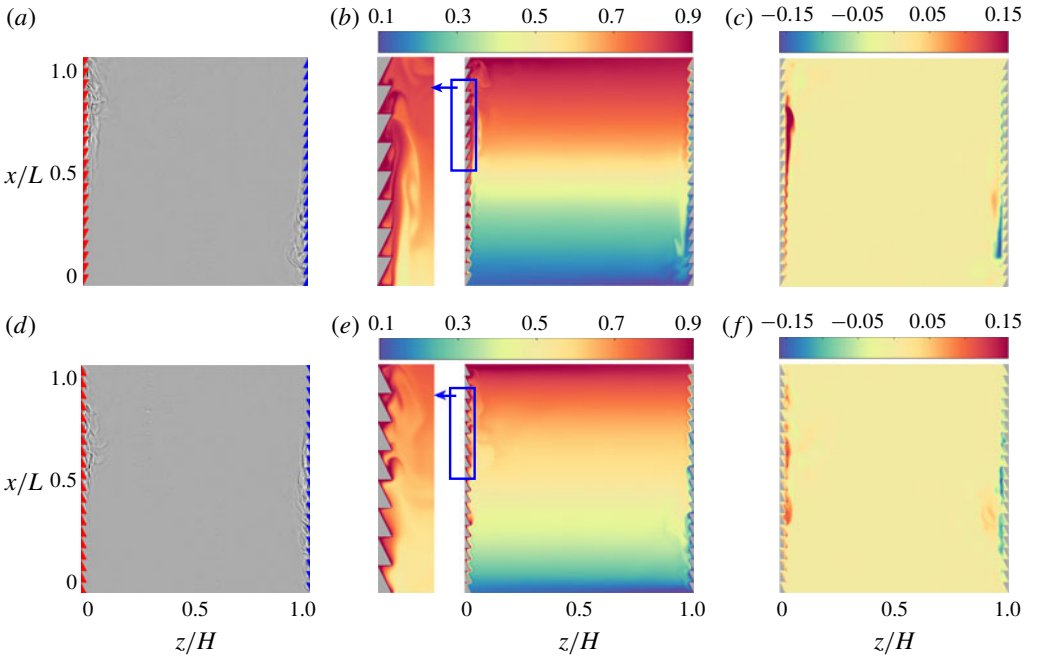

FIGURE 4. (Colour online) (*a*,*d*) Shadowgraph visualization at $Ra = 5.7 \times 10^9$ and $Pr = 4.3$ for (*a*) VC-case-A and (*d*) VC-case-B. The directions of LSCR are clockwise in both cases. The corresponding movies (supplementary movie 1 for VC-case-A and movie 2 for VC-case-B) are available at https://doi.org/10.1017/jfm.2019.446. (*b*,*e*) Instantaneous temperature field from direct numerical simulations at $Ra = 5.7 \times 10^9$ and $Pr = 4.3$ for (*b*) VC-case-A and (*e*) VC-case-B. The left-hand insets show an enlarged portion of the representative plot for the selected windows. (*c*,*f*) Instantaneous vertical velocity field from direct numerical simulations at $Ra = 5.7 \times 10^9$ and $Pr = 4.3$ for (*c*) VC-case-A and (*f*) VC-case-B. In both cases the flow is quite calm and not turbulent.

vortex flow exists in the cavity in VC-case-A, which will be discussed in § 3.3. In a word, the smaller slope of the ratchet works as an 'accelerator' to speed up the flow, whereas the steeper slope of the ratchet acts as a 'brake' to slow down the flow.

3.3. *Properties of the temperature profiles*

We discuss the temperature profiles in this section. There are several studies of the properties of the temperature profiles for turbulent thermal convection (Belmonte, Tilgner & Libchaber 1994; Zhou & Xia 2013; Ng *et al.* 2015), which show that for smooth wall case the mean temperature profile near the plate is linear. How about the time-averaged temperature profiles in vertical convection with ratchet-shaped roughness? Here we plot the time-averaged temperature profiles for both cases A (see figure 6*a*) and B (see figure 6*c*) at $Ra = 5.7 \times 10^9$ and $Pr = 4.3$. The selected portions are located at the middle of the hot plate. The solid lines, dashed lines and dashed-dot lines are for the position above the valley of the ratchet, the position at the middle of the roughness and the position near the peak of the ratchet element, respectively. As shown in figure 6(*a*), two distinct sharp gradient regions are found in the time-averaged temperature profile for VC-case-A: the one that is very close to the plate is similar to the boundary layer of the smooth case; the other one begins from

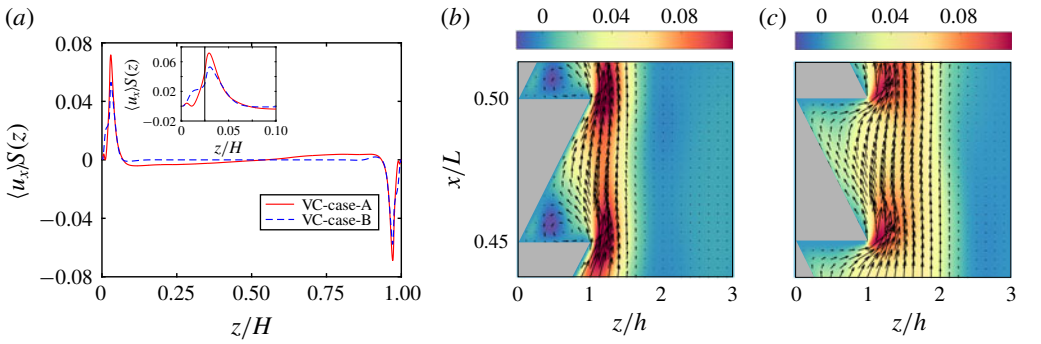

FIGURE 5. (Colour online) (*a*) The dimensionless mean vertical velocity as a function of position z/H for VC-case-A (solid line) and VC-case-B (dashed line) at $Ra = 5.7 \times 10^9$ and $Pr = 4.3$. The inset shows an enlarged portion of the plot near the roughness elements. The black line indicates where the tips of roughness elements are. (*b*) Time-averaged vertical velocity fields for VC-case-A, superposed by the velocity vectors. The selected window is located at the middle of the hot plate. (*c*) Time-averaged vertical velocity fields for VC-case-B, superposed by the velocity vector. The selected window is located at the same place as for VC-case-A.

the region neighbouring the ratchet tip and ends at the edge of the bulk. Between the two sharp gradient regions lies a plateau. However, the situation is different in VC-case-B. We note that the time-averaged temperature profile for VC-case-B is similar to that for the smooth case, for which only one linear region exists in the thin layer near the hot plate.

To illustrate the the difference of time-averaged temperature profiles between two cases, we use the 'slope' method to estimate the length scale of the thermal boundary layers (Zhou & Xia 2013; Ng *et al.* 2015; Zhang *et al.* 2018). That is, the thickness of the thermal boundary is defined as the distance at which the tangent of the mean-temperature profile at the plate crosses the bulk temperature. For VC-case-A, we can define two kinds of layer thicknesses, as reported by Zhu *et al.* (2016) in a study of Taylor–Couette flow with grooved walls. The layer between the wall and the point where the tangent of the temperature profile at the plate crosses the bulk temperature is referred to as thermal boundary layer, while the layer between the thermal boundary layer and the point where the second 'slope' crosses the bulk temperature is referred to as secondary vortex zone. Beyond this is termed as the bulk zone. As is evident in figure 6(*c*), there is only one 'slope' in the time-averaged temperature profile for VC-case-B, which means that only thickness of the thermal boundary layers can be estimated.

Figure 6(*b*,*d*) shows the thickness of the thermal boundary layer (red circles) and the thickness of secondary vortex zone (blue diamonds) as functions of x/L from mean temperature profiles. The selected windows are at the middle of the hot plates. First of all, for both cases, the ratchet-shaped roughness perturbs the thermal boundary layers, thus resulting in higher heat transfer efficiencies compared to smooth wall case. More in detail, figure 6(*b*) shows that three flow zones exist in VC-case-A, namely boundary layer, secondary vortex zone and bulk, as illustrated before. Due to the shear induced by the secondary vortex zone, the thermal boundary layer covers the ratchet surface uniformly in VC-case-A. However the situation is different in VC-case-B (see figure 6*d*), where the horizontal part of the roughness blocks the flow, which leads to

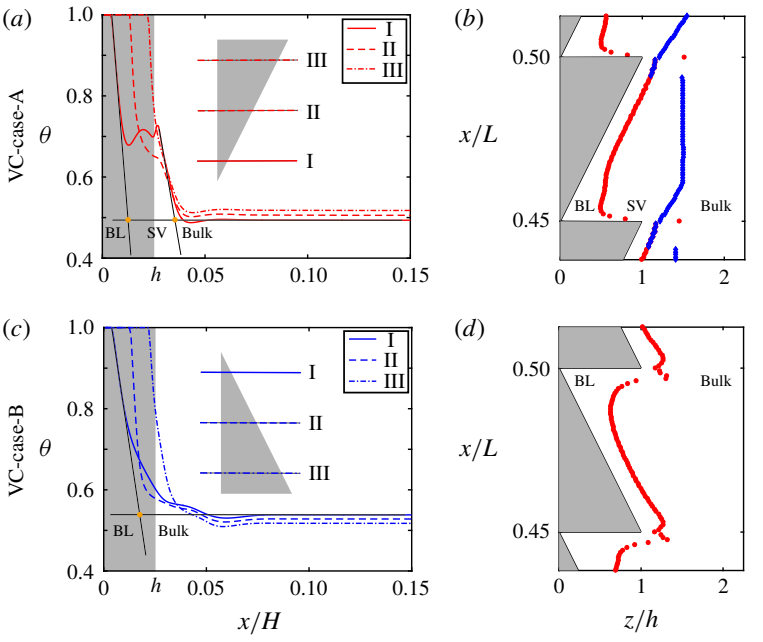

FIGURE 6. (Colour online) (*a*,*c*) Profiles of the time-averaged temperature $\langle\theta\rangle$ from direct numerical simulations at $Ra = 5.7 \times 10^9$ for (*a*) VC-case-A and (*c*) VC-case-B. The selected portions are located at the middle of the hot plate. The solid lines show the data for the position above the valley of the ratchet element, the dashed lines denote the profile at the middle of the ratchet roughness and the dashed-dot lines denote the profile near the peak of the ratchet element. (*b*,*d*) The thermal boundary layer (BL) thickness (red circles) and secondary vortex zone (SV) thickness (blue diamonds) averaged in time as functions of x/L for (*b*) VC-case-A and (*d*) VC-case-B.

the absence of secondary vortex zone (too weak to determine). Hence, VC-case-B has a thicker thermal boundary layer than VC-case-A above the valley, which explains the weaker heat transfer for the former.

Further, considering the gradient of temperature profile at the wall, we can estimate the local Nu_r based on the heat flux transported by each single roughness element (J_r). Here, Nu_r is defined as $Nu_r = J_r/(\chi\ \Delta/H)$, $J_r = 1/(W\lambda)\ \chi \int (\partial\langle\theta\rangle/\partial\hat{n})\,\mathrm{d}S$, where $\hat{n}$ is the unit vector perpendicular to the surface of the ratchet elements, and the integration $\int(\cdot)\,\mathrm{d}S$ is along the surface of roughness element. Due to the symmetry of the hot and cold boundaries, here we only calculate Nu_r at the hot plate.

As is evident in figure 7, the local Nu_r for both cases has a maximum value at the bottom of the hot plate, and then suddenly decreases with x/L increasing. After the sudden drop, the local Nu_r slightly increases with x/L increasing, then followed by a decrease until the end. Specifically, when $x/L < 0.25$, the local Nu_r for VC-case-B is slightly larger than that for VC-case-A, but the difference of local Nu_r for the two cases is relatively small. However, as x/L continues to increase, there is a significant difference for the local Nu_r between the two cases. When $x/L > 0.35$, the local Nu_r for VC-case-A is larger than that for VC-case-B. The higher local Nu_r at the upper half part of the hot plate explains the stronger global heat transport for VC-case-A. The reason for heat flux enhancement for VC-case-A is that the flow separates from the tip of the ratchet and then reattaches at the inclined surface of the next ratchet

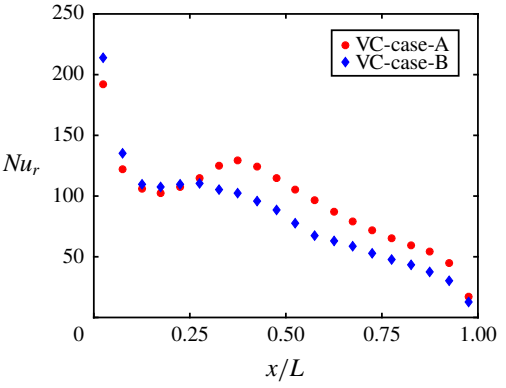

FIGURE 7. (Colour online) Local Nu_r at hot plate as a function of x/L for VC-case-A (filled circles) and VC-case-B (filled diamonds), where x/L denotes the position of each ratchet centre. The local Nu_r is defined as $Nu_r = J_r/(\chi\ \ \Delta/H)$ and $J_r = 1/(W\lambda)\ \ \chi \int (\partial\langle\theta\rangle/\partial\hat{n})\,\mathrm{d}S$, where $\hat{n}$ is the unit vector perpendicular to the surface of the ratchet element and the integration $\int(\cdot)\,\mathrm{d}S$ is along the surface of roughness element.

element at the upper part of the hot plate (see figures 4*b* and 5*b*). As is reported in Keating *et al.* (2004), in a backward-facing step the peak in heat transfer occurs just upstream of the time-averaged mean reattachment location. Similarly, in VC-case-A, the cold fluid carried by separated flow impacts the surface to cool the plate, resulting in a higher local Nu_r for VC-case-A.

3.4. *Comparisons with RBC*

Finally, we present direct comparisons of the effects of ratchet structures on heat transport between VC and RBC systems. The detailed results for RBC with ratchet roughness are demonstrated in Jiang *et al.* (2018). Here we address that the geometry of the convection cell is identical to the VC system. A small tilt of either $+3.2°$ or $-3.2°$ is introduced in the RBC in order to lock the direction of the LSCR to either case A or case B. Note that this hardly influences the heat transport properties in smooth RBC (Ciliberto, Cioni & Laroche 1996). Similar to the definition of those cases in VC, the configurations are classified into two cases. When the flow near the top and bottom plates moves along the smaller slope side of the ratchets, we refer to this situation as RBC-case-A (bottom panel of figure 8*a*). Conversely, when the flow near the top and bottom surfaces is directed towards the sharp corners of the ratchet, the configuration is referred to as RBC-case-B (top panel of figure 8*a*).

Figure 8(*b*) shows the compensated plot of $Nu/Ra^{1/3}$ versus Ra for both VC and RBC with ratchets. Most prominently, we notice that RBC has a higher heat transport efficiency than VC for the same box and the same temperature difference. This is because the flow is stronger when gravity is aligned with the temperature gradient than that when it is orthogonal. However, interestingly, RBC-case-B has a higher heat transport efficiency than RBC-case-A. In contrast, Nu enhancement in VC-case-A is larger than that in VC-case-B. What causes these differences in the trends of heat transfer augmentation between RBC and VC?

The reason for the highest heat flux in RBC-case-B is connected to the plume emissions (Jiang *et al.* 2018). In RBC, gravity is parallel to the direction of heat flux. When the flow near the wall hits the sharp corners of the ratchet, a large number

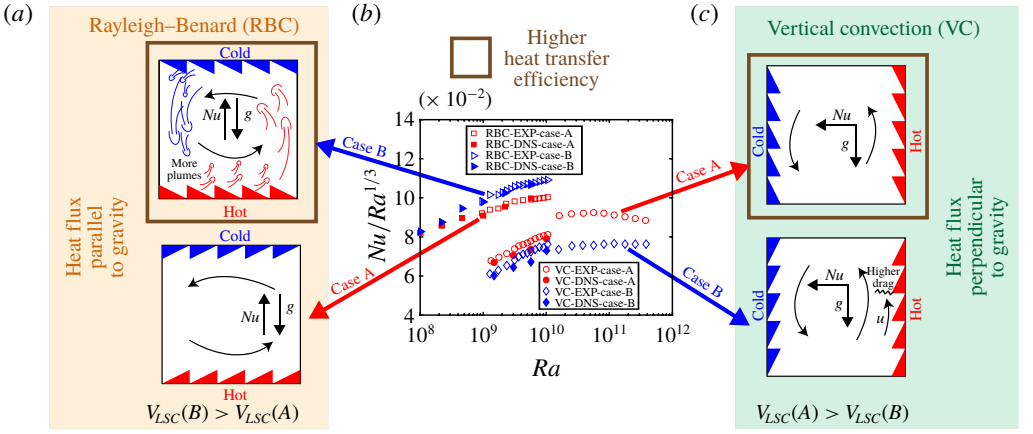

FIGURE 8. (Colour online) (*a*) Sketch of flow structures in RBC with ratchet-like roughness on the horizontal walls, which shows the process of plume emission. (*b*) The compensated plots of *Nu* with *Ra* for RBC and VC with ratchet-like roughness on hot and cold plates. The data for RBC are from Jiang *et al.* (2018). (*c*) Sketch of flow structures in VC with the ratchet-like roughness on the vertical walls, which shows the process of blocking the flow.

of plumes are detached from the boundary layer to the bulk fluid. These low-density plumes are aided by buoyancy, since in RBC the buoyancy is directed along the direction of heat flux. This explains the higher *Nu* enhancement for RBC-case-B over RBC-case-A. By means of quantitatively studying the plume emissions, we found (Jiang *et al.* 2018) that RBC-case-B has the largest number of plume emissions, followed by RBC-case-A and RBC-smooth. Further, we examine the velocity of the LSCR for RBC-case-A and RBC-case-B. It is shown that RBC-case-B has a larger roll velocity, $V_{LSC}(B) = 0.129$, than RBC-case-A, for which $V_{LSC} = 0.117$. Here V_{LSC} is defined as $V_{LSC} = (\langle u_x \rangle_S)_{max}$, where x denotes the direction parallel to gravity in RBC. Indeed in RBC, the plume emissions drive the formation of the LSCR, and more plumes not only contribute to a stronger LSCR, but also to a larger heat flux.

Unlike RBC, in VC (see figure 8*c*) the buoyancy of the plumes is parallel to the large-scale flow near the heating and cooling plates. Therefore under the effect of the buoyancy, the plumes move along the plates and do not separate. Since the flow in VC-case-B (bottom panel of figure 8*c*) has to move against the steeper slope side of the ratchet elements, it faces strong hindrance, which results in a weaker LSCR than in VC-case-A (top panel of figure 8*c*). However in RBC, instead, the buoyancy is perpendicular to the hot and cold walls. Hence the buoyancy helps the plumes flow away from the plates, resulting in plume emissions from thermal boundary to the bulk. Therefore, the ratchets serve different functions in RBC and VC. While in RBC they are the origin of strong plume emissions, in VC their role is mainly to hinder the LSCR. This, in the asymmetric ratchet cases, leads to different *Nu* enhancements between RBC and VC.

4. Conclusions

We have conducted a systematic experimental and numerical exploration of turbulent VC with asymmetric ratchet-like rough walls. Convective heat transport measurements

and flow visualizations are performed in the VC system, and the results are compared with RBC. The measured heat transport efficiency in the rough cell is found to be higher than that in the smooth cell in VC. We have identified two flow configurations, namely case A where the LSCR sweeps along the smaller slope side of the ratchet surfaces, and case B where the LSCR is directed against the steeper slope of the ratchets. The *Nu* enhancement is sensitive to the direction of LSCR over the asymmetric surface structures, i.e. VC-case-A has a higher *Nu* enhancement than VC-case-B. The measured wind Reynolds number shows that VC-case-A has a strong LSCR. In contrast, the ratchet elements in VC-case-B hinder the formation of LSCR, resulting in a weaker large-scale circulation flow. The mean vertical velocity profiles obtained from the numerical simulations quantitatively validate this interpretation. A closer analysis of mean temperature profiles indicates that the stronger LSCR in VC-case-A triggers the formation of a secondary vortex, which promotes fluid mixing inside the roughness cavity. Thus, a stronger and more efficient convective roll explains the higher *Nu* enhancement in VC-case-A than that in VC-case-B.

Further, we compare the effects of asymmetric ratchets on heat transport between two convection systems of VC and RBC. In contrast to the trend observed for VC, the *Nu* enhancement in RBC-case-B exceeds that in RBC-case-A. This is connected to the dynamics of plume emissions. In RBC-case-B, the flow near the wall hits the sharp corners of ratchet elements and leads to a greater number of plume emissions from the boundary layer to the bulk, resulting in a larger heat transfer.

This comparative study of two canonical natural convection systems, VC and RBC, has provided an improved understanding of how asymmetric wall roughness affects flow structures in varied ways to alter the global heat transport. Our findings are relevant to a range of atmospheric, oceanic and geophysical flows, as well as to engineering applications of heat exchange and flow control.

Acknowledgements

This work was supported by the Natural Science Foundation of China under grant nos. 91852202 and 11861131005, and by NWO within the programme 'Towards Ultimate Turbulence' and by MCEC programme.

Supplementary movies

Supplementary movies are available at https://doi.org/10.1017/jfm.2019.446.

REFERENCES

AHLERS, G., GROSSMANN, S. & LOHSE, D. 2009 Heat transfer and large scale dynamics in turbulent Rayleigh–Bénard convection. *Rev. Mod. Phys.* **81**, 503–537.

BATCHELOR, G. K. 1954 Heat transfer by free convection across a closed cavity between vertical boundaries at different temperatures. *Q. Appl. Maths* **12** (3), 209–233.

BELLEOUD, P., SAURY, D. & LEMONNIER, D. 2018 Coupled velocity and temperature measurements in an air-filled differentially heated cavity at $Ra = 1.2 \times 10^{11}$. *Intl J. Therm. Sci.* **123**, 151–161.

BELMONTE, A., TILGNER, A. & LIBCHABER, A. 1994 Temperature and velocity boundary layers in turbulent convection. *Phys. Rev.* E **50**, 269–279.

CHILLÀ, F. & SCHUMACHER, J. 2012 New perspectives in turbulent Rayleigh–Bénard convection. *Eur. Phys. J.* E **35**, 58.

CILIBERTO, S., CIONI, S. & LAROCHE, C. 1996 Large-scale flow properties of turbulent thermal convection. *Phys. Rev.* E **54**, R5901–R5904.

CORCIONE, M. 2010 Heat transfer features of buoyancy-driven nanofluids inside rectangular enclosures differentially heated at the sidewalls. *Intl J. Therm. Sci.* **49** (9), 1536–1546.

DOL, H. & HANJALIC, K. 2001 Computational study of turbulent natural convection in a side-heated near-cubic enclosure at a high Rayleigh number. *Intl J. Heat Mass Transfer* **44**, 2323–2344.

DOU, H.-S. & JIANG, G. 2016 Numerical simulation of flow instability and heat transfer of natural convection in a differentially heated cavity. *Intl J. Heat Mass Transfer* **103**, 370–381.

DU, Y. B. & TONG, P. 1998 Enhanced heat transport in turbulent convection over a rough surface. *Phys. Rev. Lett.* **81**, 987–990.

DU, Y. B. & TONG, P. 2000 Turbulent thermal convection in a cell with ordered rough boundaries. *J. Fluid Mech.* **407**, 57–84.

FADLUN, E. A., VERZICCO, R., ORLANDI, P. & MOHD-YUSOF, J. 2000 Combined immersed-boundary finite-difference methods for three-dimensional complex flow simulations. *J. Comput. Phys.* **161**, 35–60.

FEYNMAN, R. P., LEIGHTON, R. B. & SANDS, M. 1963 *The Feynman Lectures On Physics*, vol. 1. Addison-Wesley.

GOLUSKIN, D. & DOERING, C. R. 2016 Bounds for convection between rough boundaries. *J. Fluid Mech.* **804**, 370–386.

GROSSMANN, S. & LOHSE, D. 2001 Thermal convection for large Prandtl number. *Phys. Rev. Lett.* **86**, 3316–3319.

GVOZDIĆ, B., ALMRAS, E., MATHAI, V., ZHU, X.-J., VAN GILS, D. P. M., VERZICCO, R., HUISMAN, S. G., SUN, C. & LOHSE, D. 2018 Experimental investigation of heat transport in homogeneous bubbly flow. *J. Fluid Mech.* **845**, 226–244.

GVOZDIĆ, B., DUNG, O.-Y., ALMRAS, E., VAN GILS, D. P. M., LOHSE, D., HUISMAN, S. G. & SUN, C. 2019 Experimental investigation of heat transport in inhomogeneous bubbly flow. *Chem. Engng Sci.* **198**, 260–267.

HÄNGGI, P. & MARCHESONI, F. 2009 Artificial Brownian motors: controlling transport on the nanoscale. *Rev. Mod. Phys.* **81**, 387–442.

HUANG, S.-D., WANG, F., XI, H.-D. & XIA, K.-Q. 2015 Comparative experimental study of fixed temperature and fixed heat flux boundary conditions in turbulent thermal convection. *Phys. Rev. Lett.* **115**, 154502.

JIANG, H.-C., ZHU, X.-J., MATHAI, V., VERZICCO, R., LOHSE, D. & SUN, C. 2018 Controlling heat transport and flow structures in thermal turbulence using ratchet surfaces. *Phys. Rev. Lett.* **120**, 044501.

JOHNSTON, H. & DOERING, C. R. 2009 Comparison of turbulent thermal convection between conditions of constant temperature and constant flux. *Phys. Rev. Lett.* **102**, 064501.

KEATING, A., PIOMELLI, U., BREMHORST, K. & NESIC, S. 2004 Large-eddy simulation of heat transfer downstream of a backward-facing step. *J. Turbul.* **5**, N20.

LAGUBEAU, G., MERRER, M. L., CLANET, C. & QUÉRÉ, D. 2011 Leidenfrost on a ratchet. *Nature Phys.* **7**, 395–398.

LAVENUTA, G. 1997 Negative temperature coefficient thermistors. *Sens. J. Appl. Sens. Tech.* **14** (5), 46–55.

LINKE, H., ALEMÁN, B. J., MELLING, L. D., TAORMINA, M. J., FRANCIS, M. J., DOW-HYGELUND, C. C., NARAYANAN, V., TAYLOR, R. P. & STOUT, A. 2006 Self-propelled Leidenfrost droplets. *Phys. Rev. Lett.* **96**, 154502.

LOHSE, D. & XIA, K.-Q. 2010 Small-scale properties of turbulent Rayleigh–Bénard convection. *Ann. Rev. Fluid Mech.* **42**, 335–364.

NAREZO GUZMAN, D., XIE, Y.-B., CHEN, S.-Y., FERNANDEZ RIVAS, D., SUN, C., LOHSE, D. & AHLERS, G. 2016 Heat-flux enhancement by vapour-bubble nucleation in Rayleigh–Bénard turbulence. *J. Fluid Mech.* **787**, 331–366.

NG, C. S., OOI, A., LOHSE, D. & CHUNG, D. 2015 Vertical natural convection: application of the unifying theory of thermal convection. *J. Fluid Mech.* **764**, 349–361.

NG, C. S., OOI, A., LOHSE, D. & CHUNG, D. 2017 Changes in the boundary-layer structure at the edge of the ultimate regime in vertical natural convection. *J. Fluid Mech.* **825**, 550–572.

NG, C. S., OOI, A., LOHSE, D. & CHUNG, D. 2018 Bulk scaling in wall-bounded and homogeneous vertical natural convection. *J. Fluid Mech.* **841**, 825–850.

PAOLUCCI, S. & CHENOWETH, D. R. 1989 Transition to chaos in a differentially heated vertical cavity. *J. Fluid Mech.* **201**, 379–410.

PATTERSON, J. & IMBERGER, J. 1980 Unsteady natural convection in a rectangular cavity. *J. Fluid Mech.* **100** (1), 65–86.

VAN DER POEL, E. P., OSTILLA-MÓNICO, R., DONNERS, J. & VERZICCO, R. 2015 A pencil distributed finite difference code for strongly turbulent wall-bounded flows. *Comput. Fluids* **116**, 10–16.

PRAKASH, M., QUÉRÉ, D. & BUSH, J. W. M. 2008 Surface tension transport of prey by feeding shorebirds: the capillary ratchet. *Science* **320**, 931–934.

QIU, X. L., XIA, K.-Q. & TONG, P. 2005 Experimental study of velocity boundary layer near a rough conducting surface in turbulent natural convection. *J. Turbul.* **6**, 1–13.

ROCHE, P. E., CASTAING, B., CHABAUD, B. & HEBRAL, B. 2001 Observation of the 1/2 power law in Rayleigh–Bénard convection. *Phys. Rev.* E **63**, 045303.

SALORT, J., LIOT, O., RUSAOUEN, E., SEYCHELLES, F., TISSERAND, J.-C., CREYSSELS, M., CASTAING, B. & CHILLA, F. 2014 Thermal boundary layer near roughnesses in turbulent Rayleigh–Bénard convection: flow structure and multistability. *Phys. Fluids* **26**, 015112.

SHAKERIN, S., BOHN, M. & LOEHRKE, R. I. 1988 Natural convection in an enclosure with discrete roughness elements on a vertical heated wall. *Intl J. Heat Mass Transfer* **31** (7), 1423–1430.

SHEN, Y., TONG, P. & XIA, K.-Q. 1996 Turbulent convection over rough surfaces. *Phys. Rev. Lett.* **76**, 908–911.

SHISHKINA, O. 2016 Momentum and heat transport scalings in laminar vertical convection. *Phys. Rev.* E **93**, 051102.

SHISHKINA, O. & WAGNER, C. 2011 Modelling the influence of wall roughness on heat transfer in thermal convection. *J. Fluid Mech.* **686**, 568–582.

SMOLUCHOWSKI, M. V. 1912 Experimentally demonstrable molecular phenomena contradicting convectional thermodynamics. *Phys. Z.* **13**, 1069–1080.

STEVENS, R. J. A. M., LOHSE, D. & VERZICCO, R. 2011 Prandtl and Rayleigh number dependence of heat transport in high Rayleigh number thermal convection. *J. Fluid Mech.* **688**, 31–43.

STRINGANO, G., PASCAZIO, G. & VERZICCO, R. 2006 Turbulent thermal convection over grooved plates. *J. Fluid Mech.* **557**, 307–336.

TISSERAND, J. C., CREYSSELS, M., GASTEUIL, Y., PABIOU, H., GIBERT, M., CASTAING, B. & CHILLA, F. 2011 Comparison between rough and smooth plates within the same Rayleigh–Bénard cell. *Phys. Fluids* **23** (1), 015105.

TIWARI, R. K. & DAS, M. K. 2007 Heat transfer augmentation in a two-sided lid-driven differentially heated square cavity utilizing nanofluids. *Intl J. Heat Mass Transfer* **50** (9), 2002–2018.

TOPPALADODDI, S., SUCCI, S. & WETTLAUFER, J. S. 2017 Roughness as a route to the ultimate regime of thermal convection. *Phys. Rev. Lett.* **118**, 074503.

VAN OUDENAARDEN, A. & BOXER, S. G. 1999 Brownian ratchets: molecular separations in lipid bilayers supported on patterned arrays. *Science* **285** (5430), 1046–1048.

VERZICCO, R. & ORLANDI, P. 1996 A finite-difference scheme for three-dimensional incompressible flow in cylindrical coordinates. *J. Comput. Phys.* **123**, 402–413.

VILLERMAUX, E. 1998 Transfer at rough sheared interfaces. *Phys. Rev. Lett.* **81**, 4859–4862.

WAGNER, S. & SHISHKINA, O. 2015 Heat flux enhancement by regular surface roughness in turbulent thermal convection. *J. Fluid Mech.* **763**, 109–135.

XIE, Y.-C. & XIA, K.-Q. 2017 Turbulent thermal convection over rough plates with varying roughness geometries. *J. Fluid Mech.* **825**, 573–599.

XIN, S.-H & LE QUR, P. 1995 Direct numerical simulations of two-dimensional chaotic natural convection in a differentially heated cavity of aspect ratio 4. *J. Fluid Mech.* **304**, 87–118.

XU, F., PATTERSON, J. C. & LEI, C.-W. 2009 Transient natural convection flows around a thin fin on the sidewall of a differentially heated cavity. *J. Fluid Mech.* **639**, 261–290.

YOUSAF, M. & USMAN, S. 2015 Natural convection heat transfer in a square cavity with sinusoidal roughness elements. *Intl J. Heat Mass Transfer* **90**, 180–190.

ZHANG, Y.-Z., SUN, C., BAO, Y. & ZHOU, Q. 2018 How surface roughness reduces heat transport for small roughness heights in turbulent Rayleigh–Bénard convection. *J. Fluid Mech.* **836**, R2.

ZHOU, Q. & XIA, K.-Q. 2013 Thermal boundary layer structure in turbulent Rayleigh–Bénard convection in a rectangular cell. *J. Fluid Mech.* **721**, 199–224.

ZHU, X., OSTILLA-MONICO, R., VERZICCO, R. & LOHSE, D. 2016 Direct numerical simulation of Taylor–Couette flow with grooved walls: torque scaling and flow structure. *J. Fluid Mech.* **794**, 746–774.

ZHU, X.-J., PHILLIPS, E., SPANDAN, V., DONNERS, J., RUETSCH, G., ROMERO, J., OSTILLA-MÓNICO, R., YANG, Y., LOHSE, D., VERZICCO, R., FATICA, M. & STEVENS, R. A. J. M. 2018 AFiD-GPU: a versatile Navier–Stokes solver for wall-bounded turbulent flows on GPU clusters. *Comput. Phys. Commun.* **229**, 199–210.

ZHU, X.-J., STEVENS, R. J. A. M., VERZICCO, R. & LOHSE, D. 2017 Roughness-facilitated local 1/2 scaling does not imply the onset of the ultimate regime of thermal convection. *Phys. Rev. Lett.* **119**, 154501.